Chaos and reconnection in relativistic cyclotron motion in an elliptically polarized electric field

Duck-Hee Kwon and Hai-Woong Lee
Department of Physics, Korea Advanced Institute of Science and Technology, Taejon 305-701, Korea
(Received 13 May 1999)

A theoretical study of the relativistic cyclotron motion occurring in a uniform magnetic field and an oscillating electric field of arbitrary polarization is performed, which aims at determining the effect of the ellipticity and the strength of the electric field upon the integrability or nonintegrability of the system. Unless a circularly polarized electric field is used, the cyclotron system is nonintegrable and displays stochastic behavior in the region where resonance islands overlap. It is found, however, that the stochastic layers become increasingly thin as the polarization angle is moved closer toward $\pi/2$ (circular polarization). If the polarization angle is held fixed and the electric field amplitude is increased, the Kolmogorov-Arnold-Moser curves separating the resonance islands experience a reconnection process through which the islands are topologically rearranged. When the rearrangement is accomplished, the phase space is occupied mostly by regular trajectories. [S1063-651X(99)02710-5]

PACS number(s): 05.45.−a, 41.75.−i

I. INTRODUCTION

Charged particles moving at relativistic velocities in electric and magnetic fields are encountered often in various areas of physics including accelerator physics, plasma physics, and optics. The question concerning the integrability of the motion of such particles is of great importance, because chaotic behavior is known to have negative effects upon the performance of such devices as the cyclotron, tokamak, and free-electron laser [1–7]. A detailed investigation of the dynamics of relativistic particles may thus help find a way of suppressing chaos and thereby enhancing the performance of the devices.

It has been shown recently [8–10] that the relativistic cyclotron motion can exhibit chaos when the electric field is linearly polarized and sufficiently strong, while it is always integrable when the electric field is circularly polarized. In this paper, we carry out a detailed investigation of how the characteristics of the cyclotron motion changes, i.e., how the system changes from integrable to nonintegrable and vice versa, as the polarization state of the electric field is varied at a fixed field amplitude, or as the amplitude of the electric field is varied at a fixed angle of polarization.

II. SYSTEM

We consider the relativistic motion of a particle of mass m and charge q in a uniform magnetic field,

$$\vec{B}=B_0\hat{e}_z, \tag{1}$$

and a transverse time-periodic electric field of arbitrary polarization,

$$\vec{E}=E_0\cos\omega t\hat{e}_x+E_0\cos(\omega t-\phi)\hat{e}_y, \tag{2}$$

where $\hat{e}_i$ denotes a unit vector along the i direction. The scalar and vector potentials φ and $\vec{A}$ can be taken to be

$$\varphi=-xE_0\cos\omega t-yE_0\cos(\omega t-\phi), \tag{3}$$

$$\vec{A}=-\frac{B_0}{2}y\hat{e}_x+\frac{B_0}{2}x\hat{e}_y. \tag{4}$$

Here and throughout the paper, Gaussian units are used. The Hamiltonian for the particle is given by

$$H=\sqrt{\left(P_x+\frac{qB_0}{2c}y\right)^2c^2+\left(P_y-\frac{qB_0}{2c}x\right)^2c^2+m^2c^4}-qE_0x\cos\omega t-qE_0y\cos(\omega t-\phi). \tag{5}$$

Introducing dimensionless parameters [9]

$$\hat{x}=\frac{\omega}{c}x,\quad \hat{y}=\frac{\omega}{c}y,\quad \hat{P}_x=\frac{P_x}{mc},\quad \hat{P}_y=\frac{P_y}{mc},$$

$$\hat{t}=\omega t,\quad \hat{H}=\frac{H}{mc^2},\quad \Omega=\frac{qB_0}{mc\omega},\quad a=\frac{qE_0}{mc\omega},$$

the Hamiltonian can be rewritten as

$$\hat{H}=\sqrt{\left(\hat{P}_x+\frac{\Omega}{2}\hat{y}\right)^2+\left(\hat{P}_y-\frac{\Omega}{2}\hat{x}\right)^2+1}-a\hat{x}\cos\hat{t}-a\hat{y}\cos(\hat{t}-\phi). \tag{6}$$

This Hamiltonian can be transformed into a form having one degree of freedom by a series of three canonical transformations $(\hat{x},\hat{y},\hat{P}_x,\hat{P}_y)\rightarrow(\tilde{x},\tilde{y},\tilde{P}_x,\tilde{P}_y)\rightarrow(Q_1,Q_2,P_1,P_2)\rightarrow(q,Q,p,P)$ generated, respectively, by

$$F_2(\hat{x},\hat{y},\tilde{P}_x,\tilde{P}_y)=\left(\tilde{P}_x-\frac{\Omega}{2}\hat{y}\right)\hat{x}+\tilde{P}_y\hat{y}, \tag{7}$$

$$F_2(\tilde{x},\tilde{y},P_1,P_2)=(P_2+\Omega\tilde{x})\tilde{y}+P_1\left(\tilde{x}+\frac{P_2}{\Omega}\right), \tag{8}$$

and

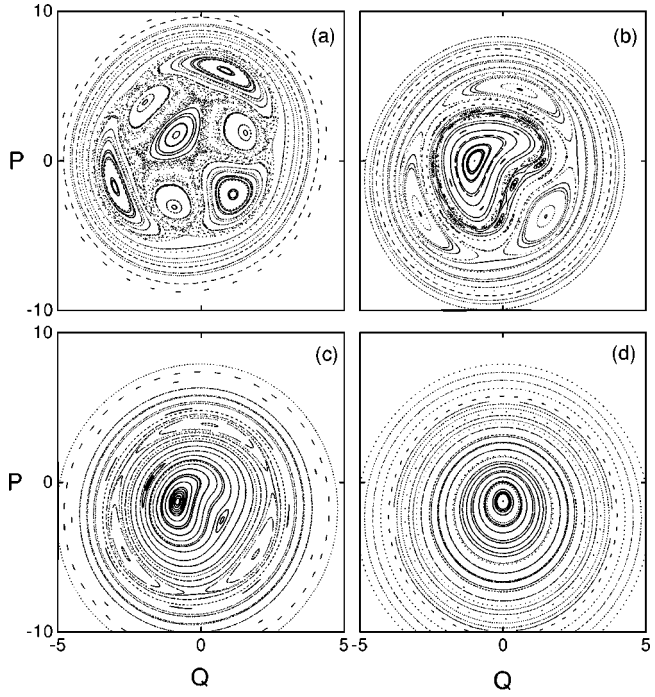

FIG. 1. Poincaré maps for the case when the dimensionless magnetic and electric field amplitudes are given, respectively, by $\Omega=2.0$ and $a=2.85$. The polarization angle ϕ is (a) 0, (b) $\pi/6$, (c) $\pi/3$, and (d) $\pi/2$.

$$F_2(Q_1,Q_2,p,P)=Q_2P+Q_1p-\frac{a}{\Omega}p\sin(\hat{t}-\phi)+aQ_1\sin\hat{t}+\frac{a^2}{4\Omega}\cos(2\hat{t}-\phi)-\frac{a^2}{2\Omega}\sin\phi\cdot\hat{t}. \tag{9}$$

The final transformed Hamiltonian takes the form

$$H=\sqrt{(\Omega Q)^2+P^2+1}+\frac{a}{\Omega}P\cos\hat{t}-aQ\cos(\hat{t}-\phi), \tag{10}$$

which leads immediately to the equations of motion

$$\frac{dQ}{d\hat{t}}=\frac{P}{\sqrt{(\Omega Q)^2+P^2+1}}+\frac{a}{\Omega}\cos\hat{t}, \tag{11}$$

$$\frac{dP}{d\hat{t}}=-\frac{\Omega^2Q}{\sqrt{(\Omega Q)^2+P^2+1}}+a\cos(\hat{t}-\phi). \tag{12}$$

In the next sections we present Poincaré maps obtained in (Q,P) space by numerically integrating Eqs. (11) and (12) for different values of the polarization angle ϕ and dimensionless electric field amplitude a. The dimensionless magnetic field amplitude Ω is held fixed at $\Omega=2.0$ in all computations.

III. POINCARÉ MAPS AT DIFFERENT POLARIZATION ANGLES

Figure 1 shows Poincaré maps for four different values of the polarization angle, $\phi=0$, $\pi/6$, $\pi/3$, and $\pi/2$, at a fixed value $a=2.85$ of the electric field amplitude. At $\phi=0$ (linear polarization), one observes chaotic orbits covering the region where the primary 3:1 resonance islands and the secondary 3:1 resonance islands overlap. The two rings of the 3:1 resonance islands, which are merged and reconnected at $a=2.85$, will eventually experience a topological rearrangement if the electric field amplitude is further increased. The details of this reconnection process [11–14] will be described in Sec. V. At $\phi=\pi/6$ and $\pi/3$, no appreciable chaotic motion is seen; in fact, there is no evidence for the formation of the secondary 3:1 resonance, while a pair of 7:3 resonances is seen to appear at $\phi=\pi/6$ and a 2:1 resonance appears at $\phi=\pi/3$. At $\phi=\pi/2$ (circular polarization), an infinity of primary 3:1 periodic orbits exists, but the island structure is not shown.

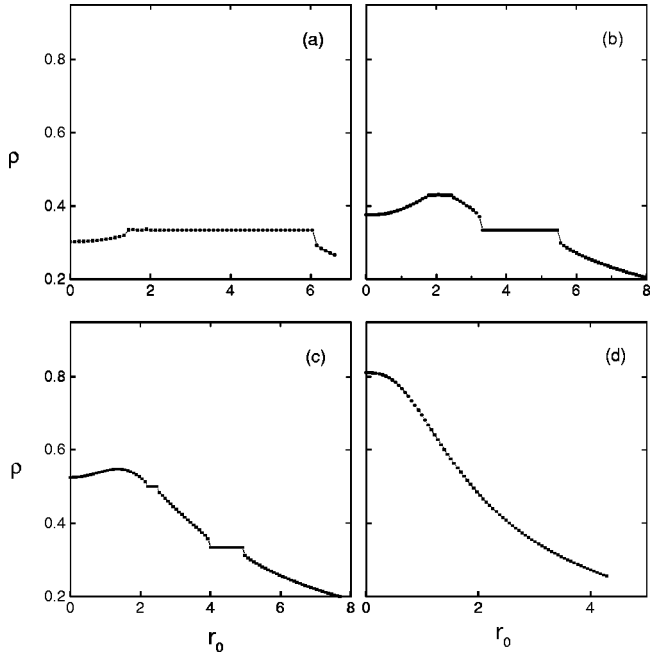

FIG. 2. Rotation number ρ about the central fixed point for the case $\Omega=2.0$ and $a=2.85$. The polarization angle ϕ is (a) 0, (b) $\pi/6$, (c) $\pi/3$, and (d) $\pi/2$.

In order to confirm the existence or nonexistence of the resonance islands seen in Fig. 1, we have calculated the rotation number

$$\rho(r_0,\theta_0)=\lim_{N\to\infty}\frac{1}{2\pi N}\sum_{n=1}^{N}(\theta_n-\theta_{n-1}), \tag{13}$$

where (r,θ) denotes the polar coordinates of (Q,P) and θ_n is calculated at time $\hat{t}=2n\pi$. The rotation number yields the average fraction of a revolution per iteration for an orbit starting at (r_0,θ_0). In Fig. 2 we show the calculated rotation number ρ about the central 1:1 resonance elliptic fixed point versus the distance r_0 of the initial point from the central fixed point, where the initial points are chosen along the line connecting the central fixed point and one of the elliptic fixed points of the primary 3:1 resonance and where the parameter values for Ω and a are chosen as in Fig. 1. Figure 2(a) drawn at $\phi=0$ shows a broad plateau of $\rho=\frac{1}{3}$ corresponding to the region where the primary 3:1 resonance is-

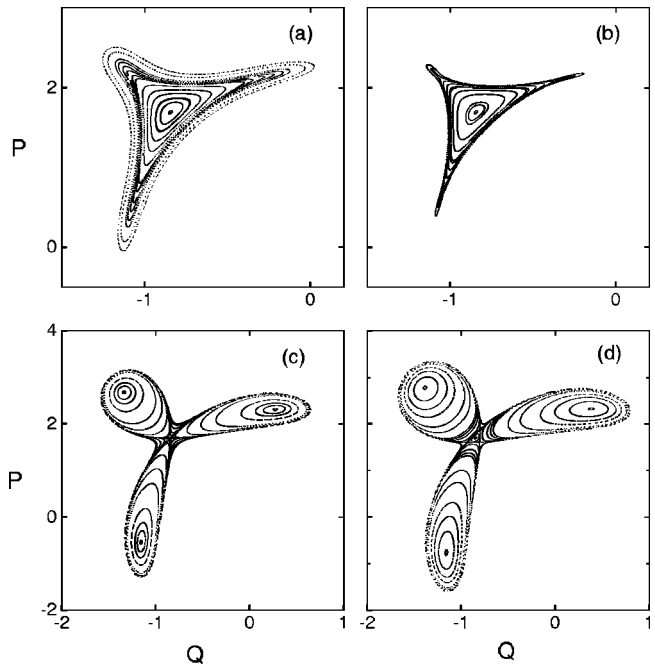

FIG. 3. Poincaré maps for the case $\phi=0$ and $\Omega=2.0$. The dimensionless electric field amplitude a is (a) 2.36, (b) 2.361 25, (c) 2.395 25, and (d) 2.41.

land and the secondary 3:1 resonance island reconnect. Figure 2(b) drawn at $\phi=\pi/6$ has a plateau of $\rho=\frac{1}{3}$ indicating the presence of the primary 3:1 resonance but no secondary 3:1 resonance, and a plateau of $\rho=\frac{3}{7}$ which upon close inspection reveals a double structure corresponding to the twin 7:3 resonance islands seen in Fig. 1(b). At $\phi=\pi/3$ the maximum value of the rotation number is increased as seen from Fig. 2(c), and the rotation number exhibits a plateau of $\rho=\frac{1}{2}$ indicating the presence of the 2:1 resonance island seen in Fig. 1(c). Another single plateau of $\rho=\frac{1}{3}$ at this angle $\phi=\pi/3$ indicates that the primary 3:1 resonance exists but not the secondary 3:1 resonance. At $\phi=\pi/2$ [Figs. 1(d) and 2(d)] no plateau is seen as the primary 3:1 resonance island has a zero size. In fact, the 3:1 periodic points exist continuously on an invariant surface [15,16], i.e., there is an infinity of 3:1 periodic orbits. Thus the map is indicative of integrable motion.

IV. BIRTH OF THE SECONDARY 3:1 RESONANCE

The primary 3:1 resonance exists for all nonzero values of the dimensionless electric field amplitude a for all polarizations. On the other hand, the secondary 3:1 resonance is born at some critical value of the field amplitude, which depends on the polarization state of the electric field. In this section we investigate the birth process of the secondary 3:1 resonance. We first present Fig. 3 in which Poincaré maps computed at $\phi=0$ and at the values of the electric field amplitude a just below and above the birth of the secondary 3:1 resonance are shown. At $a=2.36$, at which Fig. 3(a) is drawn, the secondary 3:1 resonance is not born yet. Figure 4 shows that at $a=2.36$ the rotation number about the central fixed point has a local minimum value slightly higher than $\frac{1}{3}$. Thus, at a slightly higher value $a=2.361\,25$ of the electric field amplitude, the secondary 3:1 resonance in the form of a

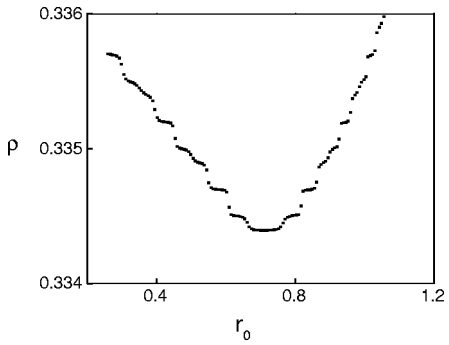

FIG. 4. Rotation number ρ about the central fixed point for the case $\phi=0$, $\Omega=2.0$, and $a=2.36$.

dimerized chain [11] or *zero dispersion nonlinear resonance* [17] appears as seen from Fig. 3(b). As a is increased to 2.395 25, the central island gets squeezed by the hyperbolic fixed points of the secondary 3:1 resonance until eventually these hyperbolic fixed points are absorbed by the central fixed point [12,18,19], as seen from Fig. 3(c). Figure 3(d) indicates that as a is increased beyond 2.395 25, the hyperbolic fixed points reappear as they move outward from the central fixed point, which results in a topological rearrangement that converts the dimerized chain into a Poincaré-Birkhoff (PB) chain [11].

The disappearance and reappearance of the hyperbolic fixed points of the secondary 3:1 resonance can also be verified by calculating the residue R defined by [16,19]

$$R=[2-\mathrm{Tr}(\mathbf{A})]/4, \tag{14}$$

where $\mathrm{Tr}(\mathbf{A})$ represents the trace of matrix $\mathbf{A}$ which governs the motion of nearby orbits of a k periodic orbit and is related with the following equations:

$$\mathbf{x}_0=\mathbf{T}^k(\mathbf{x}_0),$$

$$\Delta\mathbf{x}_{n+k}=\mathbf{A}\cdot\Delta\mathbf{x}_n, \quad \mathbf{x}=\mathbf{x}_0+\Delta\mathbf{x},$$

where $\mathbf{T}$ represents the original map. The residue takes a value $0<R<1$ for an elliptic orbit and $R<0$ or $R>1$ for a hyperbolic orbit. In Fig. 5 we show the residue of the hyperbolic fixed point of the secondary 3:1 resonance as a function of the electric field amplitude a. The residue is less than zero except in the small neighborhood about $a=2.395\,25$, which

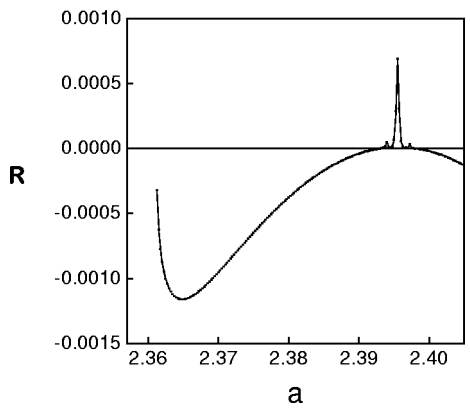

FIG. 5. Residue R of the hyperbolic secondary 3:1 resonance point vs a for the case $\phi=0$ and $\Omega=2.0$.

indicates that at $a=2.395\,25$ the absorption of the hyperbolic fixed point into the elliptic fixed point occurs.

For other polarizations of the electric field, the secondary 3:1 resonance appears at a greater value of a than that found above for linear polarization. We can estimate the value of a at which the secondary 3:1 resonance begins to appear analytically as follows. We first perform a canonical transformation

$$P=\sqrt{2\Omega J}\cos\Theta,$$

$$Q=\sqrt{\frac{2J}{\Omega}}\sin\Theta,$$

upon the Hamiltonian of Eq. (10) and obtain, for the transformed Hamiltonian,

$$H(J,\Theta,\hat{t})=\sqrt{2\Omega J+1}+\frac{a}{\sqrt{\Omega}}\sqrt{J}\{\sqrt{1-\sin\phi}\cos(\Theta-\hat{t}+\alpha)+\sqrt{1+\sin\phi}\cos(\Theta+\hat{t}+\beta)\},\tag{15}$$

where

$$\tan\alpha=\frac{\cos\phi}{1-\sin\phi},$$

$$\tan\beta=\frac{\cos\phi}{1+\sin\phi}.$$

Another transformation $(J,\Theta)\rightarrow(I,\Psi_{\pm})$ with the generating function

$$S_{+}(I,\Theta)=I(\Theta+\hat{t}+\beta)\tag{16}$$

or

$$S_{-}(I,\Theta)=I(\Theta-\hat{t}+\alpha)\tag{17}$$

leads to the Hamiltonian in the central 1:1 resonance frame,

$$H'(I,\Psi_{\pm})=\sqrt{2\Omega I+1}\pm I+\frac{a}{\sqrt{\Omega}}\sqrt{1\pm\sin\phi}\sqrt{I}\cos\Psi_{\pm},\tag{18}$$

where the fast oscillating term of Eq. (15) is ignored. We note that, when the electric field is (nearly) linearly polarized, the 1:1 resonance point rotates clockwise in (Q,P) space and the transformation with the generating function S_{-} should be taken. On the other hand, if the electric field is (nearly) circularly polarized, the 1:1 resonance point rotates counterclockwise and the transformation with the generating function S_{+} is to be chosen. The fixed point $(I_{f\pm},\Psi_{f\pm})$ of the 1:1 resonance satisfies $d\Psi_{\pm}/d\hat{t}=dI/d\hat{t}=0$, where

$$\frac{d\Psi_{\pm}}{d\hat{t}}=\frac{\Omega}{\sqrt{2\Omega I+1}}\pm1+\frac{a}{\sqrt{\Omega}}\sqrt{1\pm\sin\phi}\frac{1}{2\sqrt{I}}\cos\Psi_{\pm},\tag{19}$$

$$\frac{dI}{d\hat{t}}=\frac{a}{\sqrt{\Omega}}\sqrt{1\pm\sin\phi}\sqrt{I}\sin\Psi_{\pm}.\tag{20}$$

For the case when the transformation with the generating function S_{-} is taken, we obtain from Eq. (20) $\Psi_{f-}=0$ or π. When Ψ_{f-} is 0, the eigenvalue of the linearized equations of Eqs. (19) and (20) is imaginary and the corresponding fixed point (P_1) is elliptic. When Ψ_{f-} is π and the electric field amplitude a is below a certain critical value, two roots of I_{f-} exist, one of which gives an elliptic fixed point (P_2, imaginary eigenvalue) and the other a hyperbolic fixed point (real eigenvalue). If a is increased above the critical value, the elliptic fixed point (P_2) and the hyperbolic fixed point disappear by inverse tangent bifurcation [8,20]. For the case when the transformation with the generating function S_{+} is taken, only one root for I_{f+} exists corresponding to $\Psi_{f+}=\pi$, which gives an elliptic fixed point (P_1).

We now wish to calculate the rotation frequency $\omega_{\pm}$ about the elliptic fixed point P_1. Expanding the Hamiltonian H' about the fixed point $(I_{f\pm},\Psi_{f\pm})$, we obtain approximately [8,16]

$$H'(\Delta I_{\pm},\Delta\Psi_{\pm})\simeq\frac{\Delta I_{\pm}^2}{2G_{\pm}}+\frac{1}{2}F_{\pm}\Delta\Psi_{\pm}^2,\tag{21}$$

where

$$\frac{1}{G_{\pm}}=-\frac{\Omega^2}{(2\Omega I_{f\pm}+1)^{3/2}}-\frac{a}{4\sqrt{\Omega}}\frac{\sqrt{1\pm\sin\phi}}{I_{f\pm}^{3/2}}\cos\Psi_{f\pm},\tag{22}$$

$$F_{\pm}=-\frac{a}{\sqrt{\Omega}}\sqrt{1\pm\sin\phi}\sqrt{I_{f\pm}}\cos\Psi_{f\pm}.\tag{23}$$

The rotation frequency of the motion about the elliptic fixed point in the rotating frame is given by

$$\omega_{\pm}=\sqrt{F_{\pm}/G_{\pm}}=\left[\frac{a}{\sqrt{\Omega}}\sqrt{1\pm\sin\phi}\sqrt{I_{f\pm}}\cos\Psi_{f\pm}\left\{\frac{\Omega^2}{(2\Omega I_{f\pm}+1)^{3/2}}+\frac{a}{4\sqrt{\Omega}}\frac{\sqrt{1\pm\sin\phi}}{I_{f\pm}{}^{3/2}}\cos\Psi_{f\pm}\right\}\right]^{1/2}.\tag{24}$$

The secondary 3:1 resonance has $\omega_{-}=|\frac{1}{3}-1|=\frac{2}{3}$ and $\omega_{+}=\frac{1}{3}-(-1)=\frac{4}{3}$. The value of a at which ω_{-} is $\frac{2}{3}$ or ω_{+} is $\frac{4}{3}$ for a given polarization angle gives the electric field amplitude at which the secondary 3:1 resonance is born at that polarization angle. These values of a as calculated from Eq. (24) are listed in Table I for several different polarization angles along with the values determined numerically from Poincaré maps. The analytical values at $\phi=0$, $\pi/12$, $\pi/6$, and $\pi/4$ were estimated by computing ω_{-}, while those at $\phi=\pi/3$ and 0.49π were obtained by computing ω_{+}. The analytical values agree well with the numerical values.

TABLE I. The values of the dimensionless electric field amplitude at which the secondary 3:1 resonance is born, which are obtained analytically from Eq. (24) and numerically from Poincaré maps.

Polarization angle (ϕ)	Analytical	Numerical
0	2.35	2.361
$\pi/12$	2.72	2.76
$\pi/6$	3.32	3.41
$\pi/4$	4.31	4.36
$\pi/3$	4.92	5.19
0.49π	4.75	5.11

V. RECONNECTION OF THE PRIMARY AND SECONDARY 3:1 RESONANCE ISLANDS

As mentioned in Sec. III, the primary 3:1 resonance islands and the secondary 3:1 resonance islands undergo reconnection [11–14] as a is increased from below to above a certain critical value. In order to investigate the change of motion in phase space before and after the reconnection, we present Fig. 6. In Figs. 6(a)–6(d), we show Poincaré maps at a fixed angle of $\phi=0$ for four different values of the dimensionless electric field amplitude, $a=2.70$, 3.25, 3.40, and 3.60. At $a=2.70$ we see two rings, primary and secondary, of 3:1 resonances separated by KAM curves. The KAM curves surround the center and the three secondary islands, whereas the three primary islands reside outside the KAM curves. The secondary 3:1 resonance islands have noticeable stochastic layers arising from the overlap with numerous nearby higher-order resonance islands [16,21]. The primary 3:1 resonance islands also have such stochastic layers. We note, however, that these stochastic layers are bounded by KAM curves separating the two rings of 3:1 resonances as shown in Fig. 6(a). At $a=2.85$ the KAM curves are destroyed, the primary and secondary resonances overlap, and the chaotic orbits cover the entire overlapped region as shown in Fig. 1(a) in Sec. III. At $a=3.25$, at which Fig. 6(b) is drawn, one sees that new KAM curves appear that now surround the center and the three primary 3:1 resonance islands. The three secondary islands, on the other hand, are located outside the KAM curves. Comparing Fig. 6(b) with Fig. 6(a), it is clear that a topological rearrangement of the resonance islands has occurred. At an even higher field amplitude ($a=3.40$), the elliptic fixed points and the hyperbolic fixed points of the secondary 3:1 resonance are seen to vanish via inverse tangent bifurcation as shown in Fig. 6(c) [8,22]. The elliptic fixed points and the hyperbolic points of the primary 3:1 resonance also vanish via inverse tangent bifurcation at $a=3.60$, as shown in Fig. 6(d).

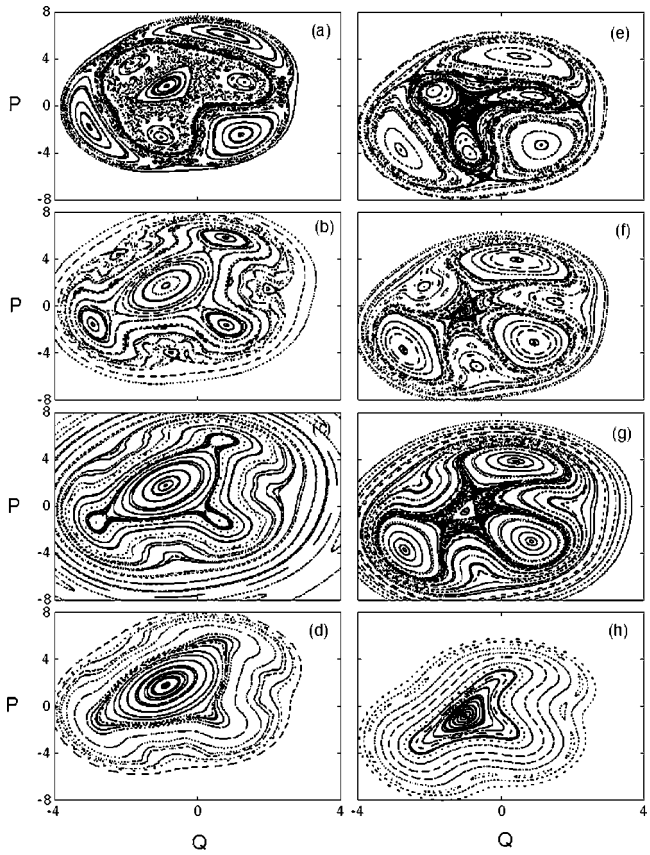

FIG. 6. Poincaré maps for the case $\Omega=2.0$. The polarization angle ϕ and the dimensionless electric field amplitude a are, respectively, (a) 0, 2.70; (b) 0, 3.25; (c) 0, 3.40; (d) 0, 3.60; (e) $\pi/6$, 3.60; (f) $\pi/6$, 3.90; (g) $\pi/6$, 4.0; and (h) $\pi/6$, 4.8.

We have also computed Poincaré maps for the case of an elliptically polarized electric field, $\phi=\pi/6$, which are shown in Figs. 6(e)–6(h). Here one finds essentially the same qualitative behavior as for the case of a linearly polarized electric field ($\phi=0$); as the field amplitude a is increased, the formation of stochastic layers which are the seed of chaos [23] and reconnection of the KAM curves separating the two rings of 3:1 resonance islands, the topological rearrangement of the primary and secondary 3:1 resonance islands after reconnection, and the vanishing of the elliptic fixed points and the hyperbolic fixed points via inverse tangent bifurcation are all observed to occur.

The reconnection process at a relatively large polarization angle is illustrated in Fig. 7, where Poincaré maps at $\phi=0.49\pi$ are shown at four different values of the electric field amplitude a just below and above the reconnection. In addition, in Fig. 8 we show the diagram of the rotation number $\rho(r_0,\theta_0)$ versus the distance r_0 [11] for the same parameter values as in Fig. 7. At $a=5.215$ we see from Fig. 7(a) that two Poincaré-Birkhoff (PB) chains which represent the primary and secondary 3:1 resonances separated by a KAM barrier appear. The rotation number diagram of Fig. 8(a) has a plateau which indicates the existence of the secondary 3:1 resonance islands. As the initial points (r_0,θ_0) are chosen along the line connecting the central fixed point and one of the elliptic fixed points of the secondary 3:1 resonance, the presence of the primary 3:1 resonance in this diagram is represented only by the point P of Fig. 8(a) having $\rho=\frac{1}{3}$. We mention here that the rotation number may not be defined in a small interval around P [24], because there is chaos near a hyperbolic fixed point. The region to the immediate left of the plateau (or to the immediate right of P) has $\rho<\frac{1}{3}$, while the region to the immediate right of the plateau (or to the immediate left of P) has $\rho>\frac{1}{3}$, which indicates that both the primary and secondary 3:1 resonances form PB chains. Figure 7(b) indicates that, when a is increased to 5.22, the separatices of the primary and secondary 3:1 resonance islands

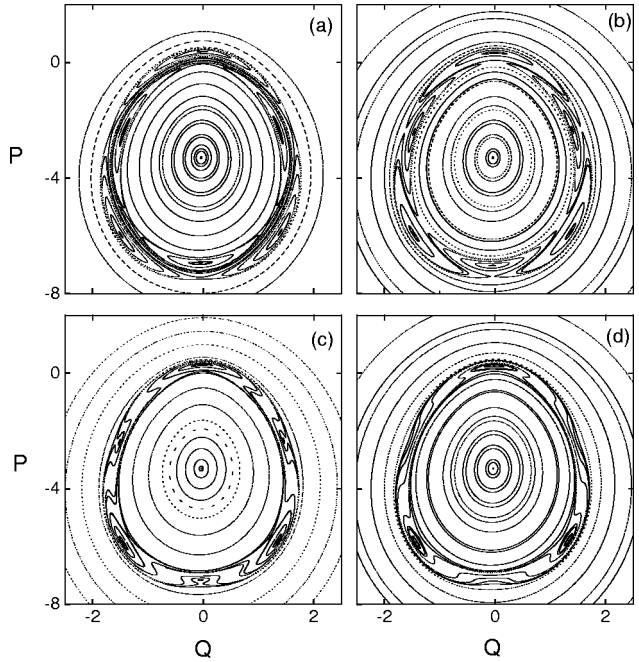

FIG. 7. Poincaré maps for the case $\phi = 0.49\pi$ and $\Omega = 2.0$. The dimensionless electric field amplitude a is (a) 5.215, (b) 5.22, (c) 5.225, and (d) 5.227.

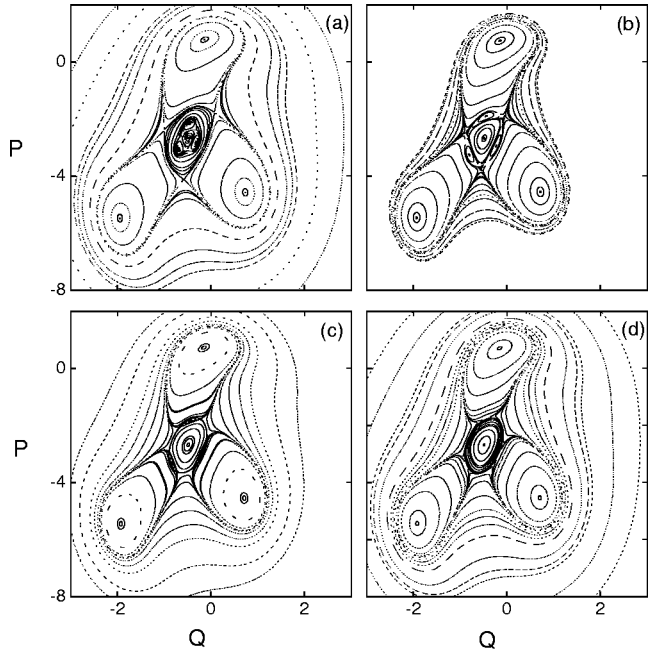

FIG. 9. Poincaré maps for the case $\phi = \pi/3$ and $\Omega = 2.0$. The dimensionlees electric field amplitude a is (a) 5.20, (b) 5.211, (c) 5.215, and (d) 5.22.

are united. The corresponding rotation number diagram of Fig. 8(b) shows a plateau surrounded by regions of $\rho < \frac{1}{3}$, indicating that the plateau and the point P which are clearly separated in Fig. 8(a) are now merged. At $a = 5.225$, we see from Fig. 7(c) that a transition from the PB chains to dimerized chains has occurred via a topological rearrangement. This transition produces in the rotation number diagram of Fig. 8(c) a sharp peak and a plateau, which indicate the presence of the primary and secondary 3:1 resonances, respectively. One sees that both the sharp peak and the plateau are surrounded by regions of $\rho < \frac{1}{3}$, confirming that two dimerized chains exist. At $a = 5.227$, we see from Fig. 7(d) that the elliptic fixed points and the hyperbolic fixed points of the secondary 3:1 resonance vanish via inverse tangent bifurcation. The rotation number diagram of Fig. 8(d) is thus characterized by the absence of the plateau of $\rho = \frac{1}{3}$.

Poincaré maps and the rotation number diagrams at a polarization angle of $\phi = \pi/3$ are presented in Figs. 9 and 10, respectively. A comparison of Figs. 9 and 10 with Figs. 7

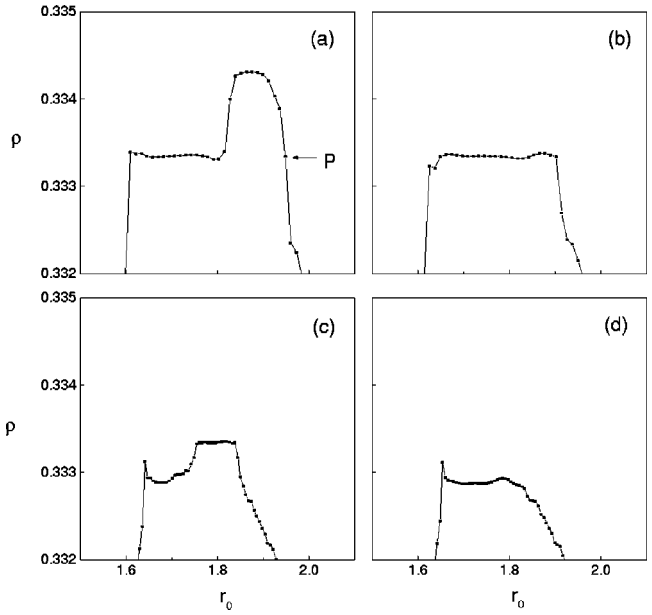

FIG. 8. Rotation number ρ about the central fixed point for the case $\Omega = 2.0$ and $\phi = 0.49\pi$. The dimensionless electric field amplitude a is (a) 5.215, (b) 5.22, (c) 5.225, and (d) 5.227.

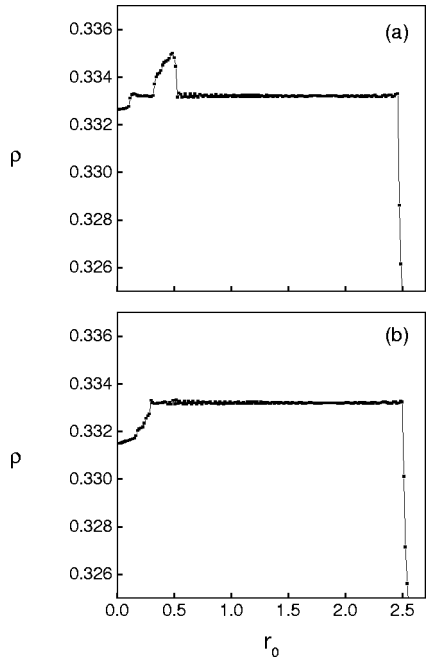

FIG. 10. Rotation number ρ about the central fixed point for the case $\Omega = 2.0$ and $\phi = \pi/3$. The dimensionless electric field amplitude a is (a) 5.20 and (b) 5.211.

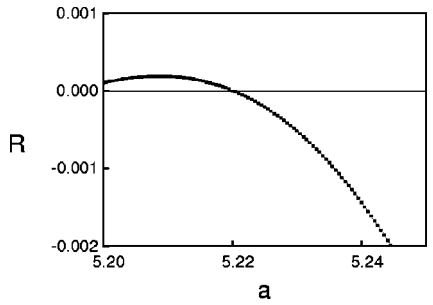

FIG. 11. Residue R of the elliptic secondary 3:1 resonance point vs a for the case $\phi=\pi/3$ and $\Omega=2.0$.

and 8 shows that there are some interesting differences between the reconnection process at $\phi=\pi/3$ and that at $\phi=0.49\pi$. From Fig. 9(a) we see that at $a=5.20$, two PB chains constitute the primary and secondary 3:1 resonances. In contrast to the situation of Fig. 7(a), the elliptic fixed points of the secondary 3:1 resonance lie along the same directions from the center as the elliptic fixed points of the primary 3:1 resonance. The rotation number diagram of Fig. 10(a) thus shows two separate plateaus. As $a=5.211$, we see from Fig. 9(b) that reconnection has occurred and thus the two plateaus are merged in Fig. 10(b). When a is further increased, the central island and the primary 3:1 islands expand and squeeze the elliptic islands of the secondary 3:1 resonance, until eventually the islands disappear and only the hyperbolic fixed points remain, as can be seen from Figs. 9(c) and 9(d). We can ascertain the vanishing of the elliptic fixed point of the secondary 3:1 resonance by invesigating the stability of the elliptic fixed point. The residue R of the elliptic fixed point of the secondary 3:1 resonance varies with a as shown in Fig. 11. For $a<5.22$, the elliptic fixed point is stable $(0<R<1)$, but for $a>5.22$ the point is unstable $(R<0)$.

We noted that different types of the reconnection process occur at $\phi=0.49\pi$ (or at ϕ close to $\pi/2$) and at $\phi=\pi/3$ (or at ϕ sufficiently away from $\pi/2$), because the elliptic fixed points of the secondary 3:1 resonance lie along the same directions from the center as the elliptic fixed points of the primary 3:1 resonance at $\phi=\pi/3$, while at $\phi=0.49\pi$ they lie along the same directions as the hyperbolic fixed points of the primary 3:1 resonance. We use the secular perturbation theory [16,25] to analyze the change in the reconnection type that occurs when the angle ϕ is changed. Choosing the generating function $S_+(I,\Theta)=I(\Theta+\hat{t}+\beta)$, we first transform the Hamiltonian of Eq. (15) to

$$\begin{aligned} H'(I,\Psi_+,\hat{t}) &= \sqrt{2\Omega I+1}+I+\frac{a}{\sqrt{\Omega}}\sqrt{1+\sin\phi}\sqrt{I}\cos\Psi_+ \\ &\quad +\frac{a}{\sqrt{\Omega}}\sqrt{1-\sin\phi}\sqrt{I}\cos(\Psi_+-2\hat{t}+\alpha-\beta) \\ &= H_0'(I,\Psi_+)+H_1'(I,\Psi_+,\hat{t}), \end{aligned} \tag{25}$$

where the fast oscillating term $H_1'(I,\Psi_+,\hat{t})$ is kept. In the vicinity of the 1:1 resonance fixed point $(I_{+f},\Psi_{+f}=\pi)$, this Hamiltonian can be approximated as

$$\begin{aligned} H'(\zeta,\vartheta,\hat{t}) &\simeq \frac{\Delta I^2}{2G_+}+\frac{1}{2}F_+\Delta\Psi_+^2+\frac{a}{\sqrt{\Omega}}\sqrt{1-\sin\phi}\sqrt{I_{+f}} \\ &\quad\times\cos(\Delta\Psi_+-2\hat{t}+\alpha-\beta+\pi), \\ &= \omega_+\zeta+\frac{a}{\sqrt{\Omega}}\sqrt{1-\sin\phi}\sqrt{I_{+f}} \\ &\quad\times\cos\left(\sqrt{\frac{2\zeta}{R}}\sin\vartheta-2\hat{t}-\delta\right), \\ &= \omega_+\zeta+\frac{a}{\sqrt{\Omega}}\sqrt{1-\sin\phi}\sqrt{I_{+f}} \\ &\quad\times\left\{\sum_{n=1}^{\infty}J_n\left(\sqrt{\frac{2\zeta}{R}}\right)\cos(n\vartheta-2\hat{t}-\delta)\right. \\ &\quad\left.+\sum_{m=0}^{\infty}(-1)^m J_m\left(\sqrt{\frac{2\zeta}{R}}\right)\cos(m\vartheta+2\hat{t}+\delta)\right\}, \end{aligned} \tag{26}$$

where

$$\Delta I=I-I_{+f}=\sqrt{2R\zeta}\cos\vartheta, \tag{27}$$

$$\Delta\Psi_+=\Psi_+-\Psi_{+f}=\sqrt{\frac{2\zeta}{R}}\sin\vartheta, \tag{28}$$

$$\delta=\beta-\alpha-\pi, \tag{29}$$

and

$$\omega_+=\sqrt{\frac{F_+}{G_+}}, \tag{30}$$

$$R=\sqrt{G_+F_+}. \tag{31}$$

G_+ and F_+ are given by Eqs. (22) and (23), and J_n denotes the Bessel function of order n. Noting that the 3:1 resonance point has the angular frequency $\frac{1}{3}-(-1)=\frac{4}{3}$ in the rotating frame, we use the second-order secular Lie perturbation theory [16,25] to obtain the Hamiltonian in the form

$$\begin{aligned} \overline{H}'(\overline{\zeta},\overline{\vartheta},\hat{t}) &= \overline{H}_0'(\overline{\zeta})+\overline{H}_1'(\overline{\zeta})+\overline{H}_2'(\overline{\zeta}) \\ &\quad+\overline{F}_2(\overline{\zeta})\cos(3\overline{\vartheta}-4\hat{t}-2\delta), \end{aligned} \tag{32}$$

where

$$\overline{H}_0'(\overline{\zeta})=\omega_+\overline{\zeta}, \tag{33}$$

$$\overline{H}_1'(\overline{\zeta})=0, \tag{34}$$

$$\overline{H}_2'(\overline{\zeta}) = -\frac{a^2}{\Omega}(1-\sin\phi) I_{+f} w_+ \times\left\{\frac{1}{\omega_+^2-4} J_1\left(\sqrt{\frac{2\overline{\zeta}}{R}}\right) J_1'\left(\sqrt{\frac{2\overline{\zeta}}{R}}\right) + \frac{1}{\omega_+^2-1} J_2\left(\sqrt{\frac{2\overline{\zeta}}{R}}\right) J_2'\left(\sqrt{\frac{2\overline{\zeta}}{R}}\right) + \frac{9\omega_+}{9\omega_+^2-4} J_3\left(\sqrt{\frac{2\overline{\zeta}}{R}}\right) J_3'\left(\sqrt{\frac{2\overline{\zeta}}{R}}\right)\right\}, \quad (35)$$

$$\overline{F}_2(\overline{\zeta}) = -\frac{a^2}{8\Omega}(1-\sin\phi) I_{+f}\omega_+ \left[\frac{1}{(\omega_+-1)(\omega_+-2)} \times\left\{J_1\left(\sqrt{\frac{2\overline{\zeta}}{R}}\right) J_2'\left(\sqrt{\frac{2\overline{\zeta}}{R}}\right) - 2J_2\left(\sqrt{\frac{2\overline{\zeta}}{R}}\right) J_1'\left(\sqrt{\frac{2\overline{\zeta}}{R}}\right)\right\} + \frac{9}{3\omega_+-2} J_3\left(\sqrt{\frac{2\overline{\zeta}}{R}}\right) J_0'\left(\sqrt{\frac{2\overline{\zeta}}{R}}\right)\right]. \quad (36)$$

In the above equations, the Bessel functions up to order 3 are kept and J_n' represents the derivative of the Bessel function with respect to the new action variable $\overline{\zeta}$. $H'(\overline{\zeta},\overline{\vartheta},\hat{t})$ can be reexpressed in the moving frame $(\hat{\zeta},\hat{\vartheta}=\overline{\vartheta}-4/3\hat{t}-2\delta/3)$ by means of the generating function $\hat{S}(\hat{\zeta},\overline{\vartheta})=(\overline{\vartheta}-4/3\hat{t}-2\delta/3)\hat{\zeta}$ as

$$H'(\hat{\zeta},\hat{\vartheta}) = \overline{H}_0'(\hat{\zeta}) + \overline{H}_2'(\hat{\zeta}) - \frac{4}{3}\hat{\zeta} + \overline{F}_2(\hat{\zeta})\cos(3\hat{\vartheta}). \quad (37)$$

The 3:1 resonance fixed point $(\hat{\zeta}_f,\hat{\vartheta}_f)$ satisfies $d\hat{\vartheta}/d\hat{t} = d\hat{\zeta}/dt = 0$, where

$$\frac{d\hat{\vartheta}}{d\hat{t}} = \omega_+ - \frac{4}{3} + \frac{\partial\overline{H}_2'(\hat{\zeta})}{\partial\hat{\zeta}} + \frac{\partial\overline{F}_2(\hat{\zeta})}{\partial\hat{\zeta}}\cos 3\hat{\vartheta}, \quad (38)$$

$$\frac{d\hat{\zeta}}{d\hat{t}} = 3\overline{F}_2(\hat{\zeta})\sin 3\hat{\vartheta}. \quad (39)$$

Equation (39) immediately yields $3\hat{\vartheta}=0$ or π. The stability of the fixed point is determined by the eigenvalue λ of the linearized equations of Eqs. (38) and (39), where

$$\lambda^2 = 9\overline{F}_2(\hat{\zeta}_f)\cos 3\hat{\vartheta}_f\left(\frac{\partial^2\overline{H}_2'(\hat{\zeta}_f)}{\partial\hat{\zeta}^2} + \frac{\partial^2\overline{F}_2(\hat{\zeta}_f)}{\partial\hat{\zeta}^2}\cos 3\hat{\vartheta}_f\right). \quad (40)$$

When the polarization angle $\phi=\pi/3$ and dimensionless electric field amplitude $a=4.93$, which is slightly greater than the value at which the secondary 3:1 resonance begins to exist, two roots of $\hat{\zeta}_f$ exist for $3\hat{\vartheta}_f=0$, both of which have positive values of λ^2 and therefore yield hyperbolic fixed points. For $3\hat{\vartheta}_f=\pi$, two roots of $\hat{\zeta}_f$ corresponding to negative values of λ^2 exist, which means that the two fixed points are elliptic. Similarly, one can find that at $\phi=0.44\pi$, two roots of $\hat{\zeta}_f$ corresponding to $3\hat{\vartheta}_f=0$ yield one elliptic and one hyperbolic fixed point, and two roots of $\hat{\zeta}_f$ corresponding to $3\hat{\vartheta}_f=\pi$ also yield one elliptic and one hyperbolic fixed point. The types of the fixed points that exist at $\phi=\pi/3$ and $\phi=0.44\pi$ are indicated in Figs. 12(a) and 12(b), respectively. It is clear that a change in reconnection type occurs as ϕ is moved from $\pi/3$ toward $\pi/2$.

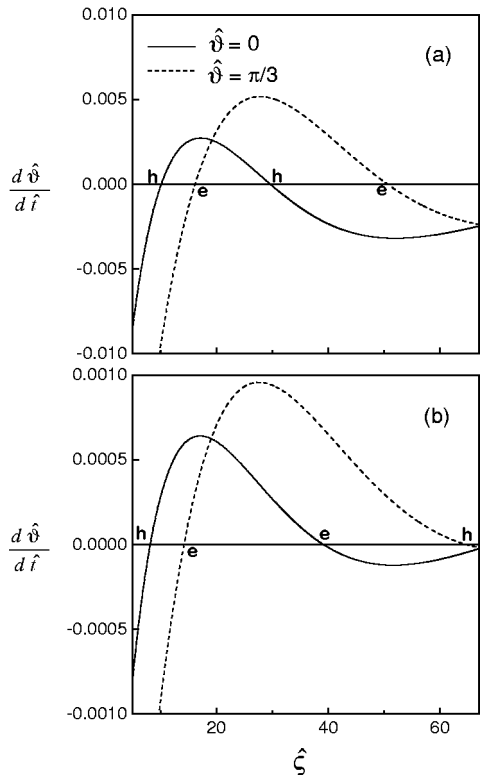

FIG. 12. The curve of $d\hat{\vartheta}(\hat{\zeta})/d\hat{t}$ vs $\hat{\zeta}$ calculated from Eq. (38). Each fixed point is marked by ''*e*'' or ''*h*'' according to whether it is elliptic or hyperbolic. The polarization angle ϕ and the dimensionless electric field amplitude a are, respectively, (a) $\phi=\pi/3$, $a=4.93$ and (b) $\phi=0.44\pi$, $a=4.774$.

Another interesting observation that can be made from Figs. 7 and 9 is that, at large angles of ϕ (e.g., $\phi=\pi/3$ and $\phi=0.49\pi$), stochastic layers are extremely thin. In fact, they are not visible in Figs. 7 and 9. This is in clear distinction to the behavior at small polarization angles, e.g., $\phi=0$ and $\phi=\pi/6$, where stochastic layers can easily be observed.

Finally we plot in Fig. 13 the critical field amplitude a_r, at which reconnection of the primary and secondary 3:1 resonances occurs, as a function of the polarization angle ϕ, obtained numerically from Poincaré maps. One sees that in general a_r increases as ϕ is increased. The local maximum at $\phi\approx 0.32\pi$ occurs probably due to the fact that at about this angle the change of the reconnection type discussed above occurs.

VI. CONCLUSION

The characteristics of the relativistic cyclotron motion in an elliptically polarized electric field depends critically upon

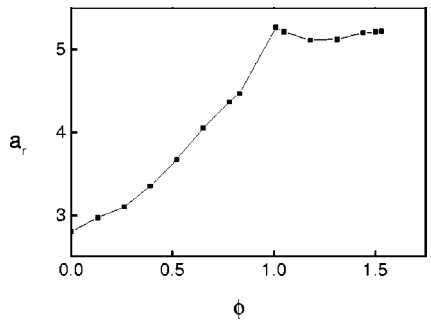

FIG. 13. The dimensionless critical electric field amplitude a_r for reconnection of the primary and secondary 3:1 resonance islands vs the polarization angle ϕ for the case $\Omega = 2.0$.

the details of the reconnection process described in the previous sections. Two important observations can be made from the data we presented. First, an increase of the electric field amplitude is not necessarily accompanied by an increase of stochastic behavior. Stochastic layers that exist in the region of overlap between nearby resonance islands, such as those of Fig. 1(a), largely disappear, when an electric field amplitude is increased and a topological rearrangement of the resonance islands is accomplished [see Figs. 6(b)–6(d)]. This is because, after the resonance islands merge and reconnect, they are reseparated by new invariant curves that prevent crossing of chaotic orbits. Thus, at electric field amplitudes higher than the reconnection threshold, the phase space is occupied mostly by regular trajectories. Second, stochastic layers become increasingly thin as the polarization is moved away from linear toward circular, until they disappear totally and the system becomes integrable when the electric field is circularly polarized. This can be clearly seen by comparing Figs. 6, 7, and 9.

We can thus conclude that cyclotron chaos can be at least partly avoided either by employing a sufficiently strong electric field to induce a topological rearrangement of islands via reconnection or by using a circularly polarized electric field or an elliptically polarized electric field sufficiently close to a circularly polarized electric field. The degrading of the cyclotron performance due to chaos can thus be largely prevented simply by choosing appropriately the amplitude and/or polarization of the driving electric field.

Finally we mention that the question concerning the polarization effect of an electric field is also an issue of great current interest in intense-field atomic physics in connection with multiphoton ionization [26–29], above-threshold ionization [30], stabilization, and high-harmonic generation [31,32]. From the fundamental viewpoint, it is natural to expect the ellipticity of the electric field to be an important factor determining the characteristics of the motion of the particle that the field drives. Our study of the cyclotron motion has direct relevance to the study of atoms in an intense laser field, in the sense that both the cyclotron and the atom in a strong laser field are examples of a strongly driven nonlinear system. It is thus hoped that our study provides useful physical insights into the question of the polarization dependence of the motion of a driven nonlinear system at a fundamental level.

ACKNOWLEDGMENTS

This research was supported in part by the Agency for Defense Development (ADD) of Korea and by the Korea Atomic Energy Research Institute (KAERI).

[1] A. E. Kaplan, Phys. Rev. Lett. **48**, 138 (1982).
[2] A. A. Chernikov, T. Tel, G. Vattay, and G. M. Zaslavsky, Phys. Rev. A **40**, 4072 (1989).
[3] G. Corso and F. R. Rizzato, J. Plasma Phys. **49**, 425 (1993).
[4] C. F. F. Karney, Phys. Fluids **21**, 1584 (1978).
[5] W. P. Leemans, C. Joshi, W. B. Mori, C. E. Clayton, and T. W. Johnston, Phys. Rev. A **46**, 5112 (1992).
[6] S. Riyopoulos and C. M. Tang, Phys. Fluids **31**, 3387 (1988).
[7] C. Chen and R. C. Davidson, Phys. Rev. A **43**, 5541 (1991).
[8] J. H. Kim and H. W. Lee, Phys. Rev. E **54**, 3461 (1996).
[9] A. Bourdier, M. Valentini, and J. Valet, Phys. Rev. E **54**, 5681 (1996).
[10] S. W. Kim and H. W. Lee, Phys. Rev. E **56**, 3602 (1997).
[11] J. P. van der Weele and T. P. Valkering, Physica A **153**, 283 (1988).
[12] G. Contopoulos, Astrophys. J. **153**, 83 (1968).
[13] J. E. Howard and S. M. Hohs, Phys. Rev. A **29**, 418 (1984).
[14] J. E. Howard and J. Humphreys, Physica D **80**, 256 (1995).
[15] L. E. Reichl, *The Transition to Chaos* (Springer-Verlag, New York, 1992).
[16] A. J. Lichtenberg and M. A. Lieberman, *Regular and Stochastic Motion* (Springer-Verlag, New York, 1983).
[17] S. M. Soskin, Phys. Rev. E **50**, R44 (1994).
[18] V. I. Arnold, *Mathematical Methods of Classical Mechanics* (Springer-Verlag, New York, 1978).
[19] J. M. Greene, R. S. MacKay, F. Vivaldi, and M. J. Feigenbaum, Physica D **3**, 468 (1981).
[20] G. Corso and F. B. Rizzato, Physica D **80**, 296 (1995).
[21] B. V. Chirikov, Phys. Rep. **52**, 263 (1979).
[22] E. Ott, *Chaos in Dynamical Systems* (Cambridge University Press, Cambridge, England, 1993).
[23] G. M. Zaslavsky *et al.*, *Weak Chaos and Quasi-regular Patterns* (Cambridge University Press, Cambridge, 1991).
[24] G. Contopoulos, Astron. J. **76**, 147 (1971).
[25] J. R. Cary, Phys. Rep. **79**, 129 (1981).
[26] P. Fu, T. J. Scholz, J. M. Hettema, and T. F. Gallagher, Phys. Rev. Lett. **64**, 511 (1990).
[27] J. A. Griffiths and D. Farrelly, Phys. Rev. A **45**, R2678 (1992).
[28] M. J. Rakovic and Shih-I. Chu, Phys. Rev. A **50**, 5077 (1994).
[29] K. Sacha and J. Zakrzewski, Phys. Rev. A **55**, 568 (1997).
[30] G. G. Paulus, F. Zacher, H. Walther, A. Lohr, W. Becker, and M. Kleber, Phys. Rev. Lett. **80**, 484 (1998).
[31] M. Protopapas, D. G. Lappas, and P. L. Knight, Phys. Rev. Lett. **79**, 4550 (1997).
[32] A. L'Huillier, K. J. Schafer, and K. C. Kulander, J. Phys. B **24**, 3315 (1991).